Infrared Contributions of X-Ray Selected Active Galactic Nuclei in Dusty Star-forming Galaxies

Arianna Brown[1,2] , Hooshang Nayyeri[1] , Asantha Cooray[1], Jingzhe Ma[1] , Ryan C. Hickox[3] , and Mojegan Azadi[4]
[1] Department of Physics and Astronomy, University of California, Irvine, CA 92697, USA
[2] Department of Physics and Astronomy, California State University, Los Angeles, CA 90032, USA
[3] Department of Physics and Astronomy, Dartmouth College, Hanover, NH 03755, USA
[4] Harvard-Smithsonian Center for Astrophysics, 60 Garden Street, Cambridge, MA 02138, USA

Abstract

We investigate the infrared (IR) contribution from supermassive black hole activity versus host galaxy emission in the mid- to far-IR spectrum for a large sample of X-ray bright active galactic nuclei (AGN) residing in dusty, star-forming host galaxies. We select 703 AGN with $L_X = 10^{42}$–10^{46} erg s^{-1} at $0.1 < z < 5$ from the *Chandra* XBoötes X-ray Survey with rich multiband observations in the optical to far-IR. This is the largest sample to date of X-ray AGN with mid- and far-IR detections that uses spectral energy distribution (SED) decomposition to determine intrinsic AGN and host galaxy IR luminosities. We determine weak or nonexistent relationships when averaging star formation activity as a function of AGN activity, but see stronger positive trends when averaging L_X in bins of star-forming activity for AGN at low redshifts. We estimate an average dust covering factor (CF) of 33% based on IR SEDs and bolometric AGN luminosity, corresponding to a Type 2 AGN population of roughly a third. We also see a population of AGN that challenge the inclination-based unification model with individual dust CFs that contradict the nuclear obscuration expected from observed X-ray hardness ratios. We see no strong connection between AGN fractions in the IR and corresponding total IR, 24 μm, or X-ray luminosities. The average rest-frame AGN contribution as a function of IR wavelength shows significant ($\sim$80%) contributions in the mid-IR that trail off at $\lambda > 30$ μm. Additionally, we provide a relation between observed L_X and pure AGN IR output for high-z AGN, allowing future studies to estimate AGN IR contribution using only observed X-ray flux density estimates.

Key words: galaxies: active – galaxies: evolution – galaxies: starburst – infrared: galaxies – X-rays: galaxies

1. Introduction

Nearly all massive galaxies are believed to host a supermassive black hole (SMBH) at their center (Kormendy & Richstone 1995; Magorrian et al. 1998; Ho 2008). Current research suggests that central black holes gain mass through a combination of both coalescence and bursts of mass accretion from the environment as the host galaxy evolves (Kauffmann & Haehnelt 2000; Volonteri et al. 2003; Somerville et al. 2008; Shankar 2009; Volonteri 2010, and references therein). The peak epoch of central black hole accretion, as the main source of active galactic nuclei (AGN), coincides with the peak epoch of star formation in the universe at $z \approx 1$–2 (Di Matteo et al. 2005; Lutz et al. 2008; Aird et al. 2010; Stevens et al. 2010; Bonfield et al. 2011; Alexander & Hickox 2012), and also major galaxy merger events (Di Matteo et al. 2005; Hopkins & Hernquist 2009; Treister et al. 2012; Ellison et al. 2013; Rosario et al. 2015). Furthermore, in our local universe there exists a tight correlation between SMBH mass and host galaxy bulge mass and stellar velocity dispersions (Ferrarese & Merritt 2000; Marconi & Hunt 2003; Gültekin et al. 2009; Kormendy & Ho 2013, and references therein), whereas higher redshift supermassive black holes have been found in smaller host galaxies than expected (e.g., Shields & Salviander 2009, and references therein). These results signify that SMBH growth and galaxy growth are co-evolutionary processes and that these processes may regulate each other over time to produce the galaxy and SMBH sizes we observe today.

Both central black hole growth and star formation rely on the abundance of cold molecular gas (Croton et al. 2006; Smith et al. 2008; Dekel et al. 2009; Dijkstra & Loeb 2009;

Bonfield et al. 2011). While cold dust and gas collapse to trigger star formation, the SMBH at the galaxy core gravitationally attracts cold gas and dust into a clumpy obscuring reservoir a few parsecs out from the SMBH, which fuels a thin, hot SMBH accretion disk with a radius typically $\lesssim$1 pc (Antonucci 1993; Tristram et al. 2007, 2009; Hopkins et al. 2012; Davies et al. 2015). The AGN feeds off the reservoir (hereby referred to as a torus; although it is now accepted that the dust is distributed in a more clumpy manner as opposed to a smooth donut structure (Nenkova et al. 2008a, 2008b; Siebenmorgen et al. 2015) with a mass accretion process that emits X-ray, UV, and optical light (e.g., see Haardt & Maraschi 1991). The X-ray, UV, and optical light is partially absorbed by the surrounding dusty toroidal structure, then re-emitted in the infrared (IR), making most AGN bright in the mid-IR, but not all AGN are X-ray bright (e.g., Treister et al. 2004; Stern et al. 2005; Daddi et al. 2007; Donley et al. 2012). The current AGN unified model posits that AGN can be classified by the orientation of the dusty torus to the observer's line of sight (Antonucci 1993; Urry & Padovani 1995): Type 1 AGN are usually observed face-on through a cavity in the torus and are typically bright in the X-ray, UV, and optical spectrum; Type 2 AGN may be intrinsically less luminous or are observed at an angle through the torus, and are thereby obscured by high column densities of dust and gas ($N_H > 1.5 \times 10^{24}$ cm^{-2}) from the observer's line of sight, enough so that most or all of the X-ray emission is absorbed and undetected (e.g., Aird et al. 2012; Lanzuisi et al. 2015). However, recent observations are challenging this scheme (e.g., see Section 3.1 of Bianchi et al. 2012) and suggesting that observational differences in obscuration between AGN are mostly driven by individual
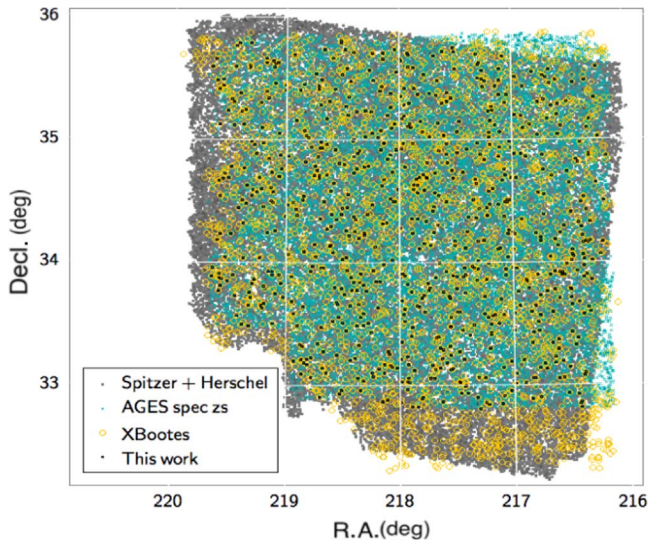
Figure 1. Survey map for the parent surveys from which our main sample is derived. Gray points mark all galaxies with a signal to noise ratio >3 in the Multiband Imaging Photometer (MIPS) 24 μm band and at least one Spectral and Photometric Imaging Receiver (SPIRE) band; blue points denote all galaxies in the AGN and Galaxy Evolution Survey (AGES) with spectroscopic redshifts; gold circles outline all of the X-ray sources in the XBoötes survey; black points mark our final sample of 703 AGN and host galaxies, which spans ~7 deg². Respective survey coverage and depths are discussion in Section 2.

SMBH accretion rates (e.g., Lusso et al. 2012; Ricci et al. 2017) or host galaxy obscuration (e.g., Goulding et al. 2012; Chen et al. 2015; Netzer 2015; Hickox & Alexander 2018).

AGN accretion and outflow mechanisms are theorized to play a major role in galaxy evolution, via heating up, consuming, and/or blasting away the host galaxy's remaining cold gas and dust necessary to create new stars, thereby triggering a star formation quenching phase (Di Matteo et al. 2005; Hopkins et al. 2006; Fabian 2012; Harrison et al. 2014, and references therein). In observations, some AGN feedback processes are instantaneously strong enough to affect star formation in the host galaxy (e.g., Reeves et al. 2009; Rupke & Veilleux 2011; Sturm et al. 2011, but also see Leung et al. 2017); however, the exact contribution of the AGN phase to the physical properties of galaxies, compared to other mechanisms from stellar processes, is still not well understood (e.g., Silk & Nusser 2010; Diamond-Stanic et al. 2012; Gabor & Bournaud 2014; Geach et al. 2014), particularly for the most powerful AGN (e.g., Rosario et al. 2012; Stanley et al. 2015). To study the effect of powerful AGN on their host galaxies, it is necessary to have a large statistical sample of AGN with multiband observations to individually derive and constrain their physical properties.

One of the main degeneracies in determining the evolutionary relationship between AGN and host galaxy star formation lies in their mutual obscuration by warm dust (Lutz et al. 2008; Delvecchio et al. 2015; Symeonidis et al. 2016). The radiation originating from warm dust in stellar nebulae and from the obscuring torus around AGN are both bright in the mid- to far-IR spectrum and thus necessary to disentangle prior to using IR radiation as an indicator for any host galaxy dust properties, including measurements of dust temperatures, host galaxy stellar mass, and star formation rates (SFRs); without this decomposition, there is a risk of measurement overestimation and, therefore, an increase in uncertainties. AGN accretion and outflow mechanisms release a large amount of

energy detectable at nearly all wavelengths, in particular X-rays from the accretion disk (see Brandt & Alexander 2015, for a review of AGN viewed in the X-ray spectrum) and radio signatures from synchroton radiation (e.g., Miley 1980; Blandford & Payne 1982; Condon et al. 1995; Jorstad et al. 2005). These features are the most commonly utilized as identifiable signatures that could be used to distinguish AGN from their host galaxies (Mushotzky 2004; Donley et al. 2005; Del Moro et al. 2013; Brandt & Alexander 2015).

Observational studies and models of IR spectral energy distributions (SEDs) for local AGN reveal radiative flux densities that generally increase through the mid-IR then rapidly decline starting somewhere between $40\,\mu m < \lambda < 100\,\mu m$ out to submillimeter wavelengths (Mullaney et al. 2011). Prior to the *Herschel Space Observatory* (Pilbratt et al. 2010), observations were limited out to $\lambda < 200\,\mu m$ only for a small sample of very far-IR bright, mostly local objects (e.g., Omont et al. 2001; Haas et al. 2003). *Herschel* has been instrumental in constraining the dust SEDs for large samples of local and high redshift AGN and star-forming galaxies, revealing a universe that is optically obscured by dust and therefore undetected at shorter wavelengths (e.g., Casey et al. 2014; Mullaney et al. 2015; Symeonidis et al. 2016, and references therein).

In this paper, we use multiwavelength IR observations from the *Herschel Space Observatory* (Griffin et al. 2010; Poglitsch et al. 2010) combined with the *Spitzer Space Telescope* (Werner et al. 2004), along with optical wide-area observations, and X-ray data from the *Chandra X-ray Observatory* (Weisskopf et al. 2002) to construct the AGN and host galaxy SEDs and explore the warm dust properties in the context of AGN accretion activity. We focus on X-ray selected AGN in the wide 9.3 deg² Boötes legacy field (Jannuzi & Dey 1999) with mid- and far-IR counterparts detected by *Herschel* and *Spitzer* (Ashby et al. 2009; Oliver et al. 2012). The rich amount of data in the IR allows us to avoid the uncertainties that arise from single-band SED fitting. Furthermore, the multiwavelength detections allow us to reliably use SED decomposition models to isolate AGN contribution in the IR, reducing the likelihood of AGN contamination when estimating host galaxy properties.

This paper is organized as follows. Section 2 describes the multiwavelength survey data used in this analysis. Section 3 details the AGN sample selection procedure. In Section 4, we discuss the derivation of AGN and host galaxy properties and the results in the context of other published studies; Section 5 provides a summary of this work. Throughout this study, we assume a cosmology with $H_0 = 70\,\mathrm{km\,s^{-1}}$, $\Omega_m = 0.3$, and $\Omega_\Lambda = 0.7$.

2. Multiwavelength Data

The survey observations used in this study are centered in the Boötes field at $\alpha = 14^{h}30^{m}05\overset{s}{.}71$, $\delta = +34°16'47''\!.5$ (Jannuzi & Dey 1999). We use publicly available photometric catalogs ranging from optical to far-IR wavelengths, complemented with X-ray data and spectroscopic redshifts, with known active galaxies (Ashby et al. 2009) and clusters of AGN (Brand et al. 2006). The multiwavelength observations cover different areas across the Boötes field (see Figure 1). Table 1 summarizes the data used and respective approximate field coverage.

Table 1
Population Counts and Field Coverage of the Multiwavelength Flux Catalogs Used to Generate 703 Individual SEDs

| Name	Bands	Survey Size	N Detected in Sample
XBoötes Murray et al. (2005)	0.5–7 keV	$\sim$9.3 deg^2	703
NDWFS Jannuzi & Dey (1999)	B_w, R, I, and K	$\sim$9.3 deg^2	652
IR Boötes Imaging Survey Gonzalez et al. (2010)	H and J	$\sim$9.3 deg^2	$\sim$325
SDWFS Ashby et al. (2009)	3.6, 4.5, 5.8 and 8.0 μm	$\sim$10 deg^2	$\sim$330
HerMES MIPS Oliver et al. (2012)	24 μm	$\sim$10 deg^2	703
HerMES PACS Oliver et al. (2012)	110 and 170 μm	$\sim$3 deg^2	138 and 181
HerMES SPIRE Oliver et al. (2012)	250, 300, and 500 μm	$\sim$8.5 deg^2 shallow, $\sim$3 deg^2 deep	489, 398, and 159
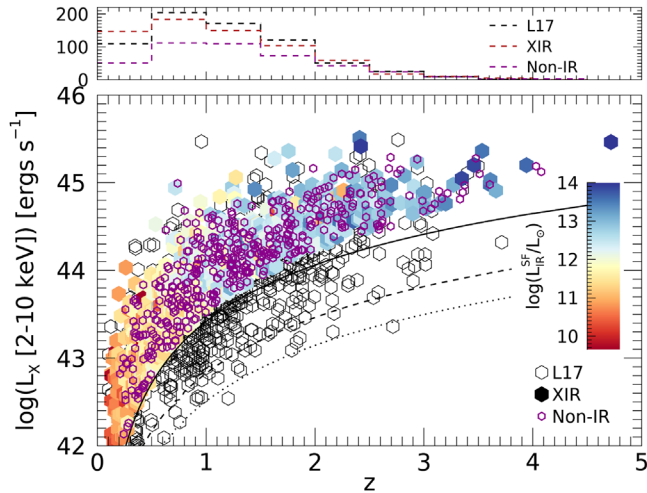
Figure 2. Distribution of rest-frame X-ray luminosities and spectroscopic redshifts for our AGN sample. The solid circles are the 703 X-ray AGN with *Spitzer* 24 μm and far-IR *Herschel* detections. Colors represent rest-frame, IR luminosities corrected for AGN contamination derived from individual respective SEDs (see Section 3). The purple circles are the 425 X-ray AGN without mid- and far-IR detections. The black empty circles are the AGN used for analysis in L17. The black solid line represents the X-ray flux limit of the *Chandra* XBoötes survey (Murray et al. 2005); for comparison, the dashed and dotted lines mark the sensitivity limits of the *XMM-Newton* (Brusa et al. 2010) and *Chandra* (Civano et al. 2016) surveys in the COSMOS field, respectively. Shown in the top panel is the number of sources in our X-ray and far-infrared detected (XIR) sample (red), non-IR sample (purple), and in L17 (black) in redshift bins of size 0.5.

The wide-area XBoötes survey provides us with a unique opportunity to probe a large population of the most powerful AGN, half of which are also embedded in galaxy powerhouses with total IR luminosities (L_{IR}) greater than $10^{12}\,L_{\odot}$ (also known as ultra-luminous IR galaxies or ULIRGs). Some weakly accreting AGN and AGN obscured by Compton thick hydrogen column densities ($N_H > 1.5 \times 10^{24}\,\mathrm{cm}^{-2}$) may be missed by X-ray surveys (e.g., Aird et al. 2012; Lanzuisi et al. 2015). However, studies confirm no single waveband can be used to select a complete sample of AGN, and X-ray detections remain one of the most reliable identification methods (e.g., Barmby et al. 2006; Mendez et al. 2013; Brandt & Alexander 2015; Cowley et al. 2016; Ellison et al. 2016; Azadi et al. 2017, and references therein).

2.1. X-Ray Data

Our AGN sample is selected from the *Chandra* XBoötes Survey, a 5 ks X-ray survey of the 9.3 deg^2 Boötes Field as defined in the NOAO Deep Wide-Field Survey (NDWFS;
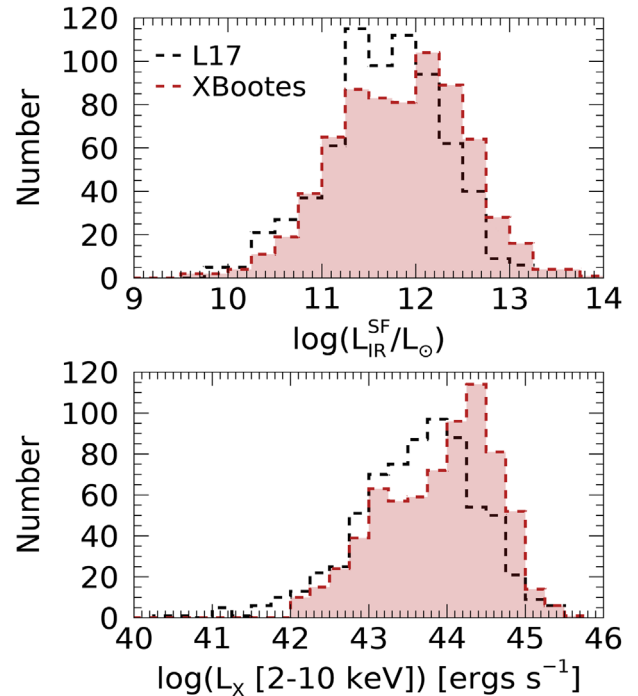
Figure 3. Distributions of AGN and host galaxy properties comparing this sample (red) and Lanzuisi et al. (2017) (L17; black) samples. *Top*: Histogram of rest-frame, AGN-corrected IR luminosities in bins of 1 dex, with median IR luminosities of 1.95×10^{45} erg s^{-1} and 2.69×10^{45} erg s^{-1} for L17 and our sample, respectively. *Bottom*: Histogram of rest-frame X-ray luminosities in bins of 1 dex; our sample has a slightly higher median X-ray luminosity of $L_X = 1.07 \times 10^{44}$ erg s^{-1} compared to the L17 median X-ray luminosity of $L_X = 4.79 \times 10^{43}$ erg s^{-1}.

Murray et al. 2005). This survey covers the full area defined by NDWFS with 126 individual 5 ks contiguous pointings at uniform observational depths of $f_{0.5-7\mathrm{keV}} \sim 8 \times 10^{-15}$ erg s^{-1} cm^{-2}, yielding 3293 point sources with four or more counts. Rest-frame X-ray luminosities are determined by the following equation (Alexander et al. 2003):

$$L_X = 4\pi \times D_L^2 \times F \times (1+z)^{\Gamma-2} \qquad (1)$$

where D_L is the luminosity distance, F is the hard band X-ray flux, z is the redshift, and a photon index of $\Gamma = 1.9$, which is typical for an unabsorbed X-ray luminous AGN (e.g., Nandra & Pounds 1994; Vignali et al. 2005). To remain consistent in comparison to other studies, we translate our full band 0.5–7 keV luminosities to 2–10 keV hard band luminosities with a conversion factor of 0.78, which is the ratio of respective intensities over each keV energy range for $\Gamma = 1.9$. Due to the shallow nature of the

XBoötes Survey, spectral fitting to correct for X-ray absorption is difficult or unachievable at an individual level for ~90% of our sources (see Kenter et al. 2005; Murray et al. 2005, for a more detailed discussion), so we leave the observed fluxes to be interpreted at face value. We select sources with X-ray luminosities $L_X > 10^{42}$ erg s^{-1} as lower luminosity sources may contain contamination from host galaxy processes (e.g., supernovae, X-ray binaries, and massive stellar outflows; Ranalli et al. 2003; Lehmer et al. 2010; Mineo et al. 2012a, 2012b). The X-ray survey depth of this study allows us to probe a larger population of the brighter end of the AGN luminosity function (see Figure 2). Figure 3 (bottom) displays the X-ray population distribution of this sample. The wider coverage of the XBoötes Survey allows us to study a large sample of powerful AGN with 50% of the 703 selected sources residing at or above $L_X = 1.07 \times 10^{44}$ erg s^{-1}; similar studies using surveys that may be deeper but cover smaller areas in the sky yield populations of weaker AGN; for example, Lanzuisi et al. (2017) (L17, hereafter) analyzed 692 X-ray selected AGN in the COSMOS field (Scoville et al. 2007) with a median $L_X = 4.79 \times 10^{43}$ erg s^{-1}.

2.2. IR Data

Mid-IR and far-IR fluxes are collected from Data Release 4 of the *Herschel* Multi-tiered Extragalactic Survey[5] (HerMES; Oliver et al. 2012). Far-IR observations were taken by the *Herschel* SPIRE at 250, 350, and 500 μm (Griffin et al. 2010), and the *Herschel* Photoconductor Array Camera and Spectrometer (PACS) 110 and 170 μm (Poglitsch et al. 2010) bands; mid-IR observations were completed by the *Spitzer* MIPS at 24 μm (Rieke et al. 2004). Fluxes for all five *Herschel* bands used in the HerMES survey are recorded on positions defined by MIPS 24 μm priors with a respective 5σ detection limit at ~0.3 mJy. The HerMES SPIRE campaign consisted of a combination of both deep and shallow observations: the center ~3 deg^2 region is deeper and reaches 5σ detection limits at 13.8, 11.3, and 16.4 mJy at 250, 350, and 500 μm, respectively; the outer ~8.5 deg^2 region surrounding the center reaches 5σ detection limits at 25.8, 21.2, and 30.8 mJy for the 250, 350, and 500 μm bands, respectively. The PACS observations occurred over the center ~3 deg^2 of the Boötes region reaching 5σ depths of 49.9 and 95.1 mJy for the 110 and 170 μm bands, respectively. Uncertainties in this analysis include both instrumental and confusion noise; we refer the reader to Roseboom et al. (2010) for a more detailed description of flux uncertainty determinations in the HerMES catalogs.

Near- and mid-IR catalogs were compiled from the *Spitzer* Deep, Wide-field Survey (SDWFS) (Ashby et al. 2009), which used all four channels of the *Spitzer* Infrared Array Camera (IRAC) (Fazio et al. 2004) to image the entire ~10 deg^2 Boötes field. SDWFS is a combined four epoch survey that contains ~10^5 sources per band detected at 5σ depths of 19.77, 18.83, 16.50, and 15.82 Vega mag at 3.6, 4.5, 5.8, and 8.0 μm, respectively. We also use *J* and *H* band data from the NEWFIRM Infrared Boötes Imaging Survey (Gonzalez et al. 2010), which reaches 5σ limits of 22.05 and 21.30 Vega mag, respectively; and optical B_w, R, I, and K band data from the NDWFS survey (Jannuzi & Dey 1999) reaching 5σ depths[6] at

26.6, 26.0, 26.0, and 21.4 AB mag, respectively. For all IR bands, we consider source detections at $>3\sigma$.

2.3. Redshifts

Spectroscopic redshifts are extracted from AGES (Kochanek et al. 2012), an optical spectroscopic and photometric redshift survey for optically selected sources in 7.7 deg^2 of the Boötes field. We limited our sample to spectroscopic redshifts in the range $z > 0.1$ (Figure 2) to avoid the uncertainties associated with photometric redshifts and avoid contamination by local AGN and ULIRGs.

To investigate the evolution of AGN and galaxy properties with redshift, we complete our analysis over five redshift intervals and consider the X-ray–IR relationship in each respective interval. The following redshift intervals are designed so that each interval has a sufficient number of sources (~90–200) to create several statistically significant bins within that range: z = 0.1–0.4, 0.4–0.8, 0.8–1.2, 1.2–2, and 2–5. These redshift bins (z-bins) are consistent in comparison with several other similar studies, and contain 95, 178, 140, 195, and 95 sources, respectively.

3. AGN Sample Selection

The final sample used in this study consists of powerful AGN with spectroscopically confirmed redshifts, and a detection in one *Herschel* SPIRE or PACS band. Since all objects in the HerMES campaign are based on *Spitzer* MIPS priors, it follows that every object in our sample has at least one 24 μm detection as well as one *Herschel* detection. We achieve this sample, dubbed the XIR sample, through the following methods.

We matched X-ray AGN to IR counterparts and spectroscopic redshifts using a nearest neighbor matching technique. First, X-ray sources were matched to the AGES redshift catalog using a 1″ search radius on their optical coordinates from Brand et al. (2006), with a spurious match rate estimated at <1%. We were able to use such a small search radius confidently due to prior work by Brand et al. (2006) who used a Bayesian matching scheme to determine optical counterparts for 98% of the X-ray sources in the XBoötes survey under a 1″ search radius. We note that AGES redshifts were determined using optical spectroscopy, and as such this study explores the properties of brighter, less dust obscured active galaxies. We also note that the AGES misses ~2 deg^2 of the XBoötes and HerMES survey (Figure 1), removing 10% of X-ray sources as possible candidates for this study. Near-IR and optical data were matched to the MIPS 24 μm coordinates from the HerMES catalog (Oliver et al. 2012), using a 3″ search radius, which corresponds to the *Spitzer* MIPS 24 μm half width at half maximum. Finally, we matched the MIPS 24 μm coordinates to the AGES coordinates. Again, we estimate a spurious match rate of <1% when matching IR data together, and once more when matching IR data to X-ray sources with spectroscopic redshifts.

Prior to fitting an SED, we require an object to have a 24 μm detection and a detection in one of the *Herschel* bands. The far-IR survey was defined on the coordinates for sources detected at 24 μm, thus any Boötes source detected by *Herschel* will also have a measurement at 24 μm. Even though *Herschel* observational depths varied across the inner and outer region of the survey area, we still find a uniform density of ~100 AGN
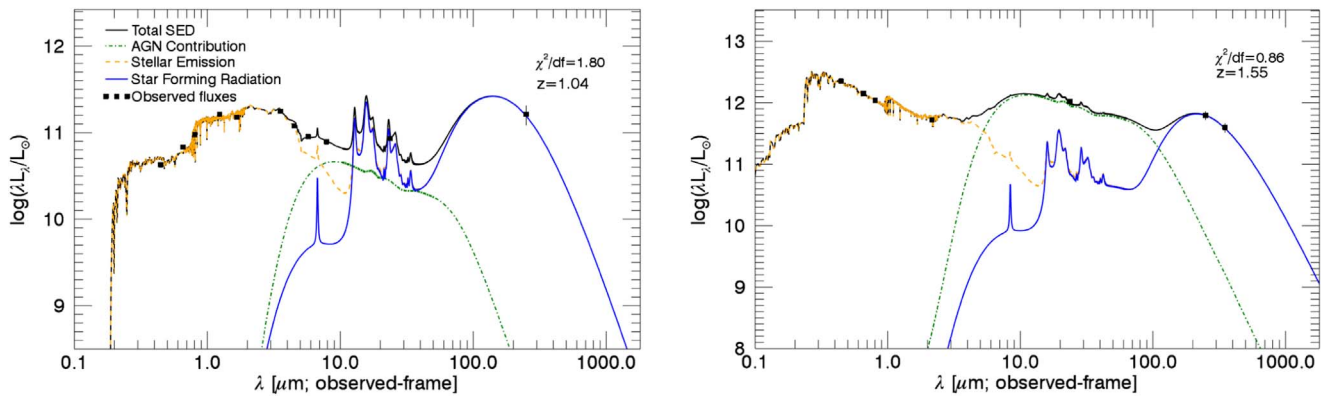
Figure 4. Example SEDs generated by SED3FIT (Berta et al. 2013). The dashed gold line is the stellar emission contribution, the blue line is the radiation contributed by star formation processes, the green dashed line is the contaminating radiation from the AGN, including the heated dusty torus surrounding the black hole, and the black line is the total SED or the summation of the three components. Left: SED for a galaxy with star formation processes dominating the mid- to far-IR spectrum. Right: In this SED, the AGN component provides the most contribution in the mid-IR (and some of the far-IR) spectrum that would typically be attributed to star formation processes.

per square degree that satisfy our selection criteria. Additionally, due to the work by Brand et al. (2006), the majority (∼93%) of the sample also has an optical detection.

The mid- and far-IR photometry requirement is unique to this work. Comparable studies required only one mid- or far-IR detection or relied on stacking techniques and photometric upper limits to supplement, creating large uncertainties when generating AGN SEDs, particularly on the Wien side of the far-IR SED corresponding to dust emission (e.g., Mullaney et al. 2012; Stanley et al. 2015; Lanzuisi et al. 2017). With the mid- and far-IR requirement, we can better constrain dusty torus emission for powerful AGN and host star-forming galaxies.

This study is based on the 703 X-ray sources in the Boötes field that have intensive multiband data to fit their individual SEDs (see Table 1 for exact counts per band). Generating individual SEDs allows us to avoid the restrictions and uncertainties related to stacking and gives us the freedom to disentangle AGN and host galaxy radiation components for each respective source. Using SED3FIT (Berta et al. 2013), a multicomponent SED fitting tool, we decompose each galaxy's emissions in the IR spectrum and use the appropriate rest-frame, IR luminosity integrated from 8–1000 μm as an indicator of host galaxy star formation rate (SFR). SED3FIT is based off of the da Cunha et al. (2008) MAGPHYS code and employs a combination of three galaxy radiation processes: stellar emission, warm and cold dust emission from star formation regions, and AGN emission. SED templates are fitted to measured fluxes first using the stellar and star-forming components only, then AGN templates are varied to fill in photometric gaps and further reduce the χ^2. We use the 10 AGN templates provided with SED3FIT, which were selected to cover the wide range of AGN found in the full Fritz et al. (2006) library. These 10 templates span Type 1, intermediate, and Type 2 AGN, with a variety of optical depths ranging from 0.1–6, as viewed face-on or edge-on. All 10 of the templates have a fixed torus opening angle of $\Theta = 100°$, corresponding to an intrinsic covering factor (CF) of 75% (see Section 4.3 for details on CFs). Each AGN template can be broken down into three components: dust scattering emission, dust thermal emission, and nuclear accretion disk emission. The former two AGN components combined are attributed to the warm, dusty clumpy structure that surrounds the SMBH and accretion

disk. See Figure 4 for two example SEDs generated from our sample (left: star formation dominant, right: AGN emission dominant).

To correct for contaminating AGN radiation, we subtract the dusty torus and accretion disk emission from the total SED of a source. The resulting IR luminosity is attributed to star formation and is hereby represented as $L_{\rm IR}^{\rm SF}$, while the subtracted IR AGN luminosity is referred to as $L_{\rm IR}^{\rm AGN}$; Figure 3 (top) shows our resulting population distribution of IR luminosities attributed to star formation processes. This procedure applies to 98% of our sample, as 13 sources are not fitted with an IR AGN component by SED3FIT. The physical characteristics derived from this procedure will be available for all 703 sources on Vizier.[7]

Out of the remaining 2.6k XBoötes sources not used in our XIR sample, we also find 425 X-ray AGN with spectroscopic redshifts but no *Spitzer* MIPS and *Herschel* counterparts (marked as purple circles in Figure 2) with a similar X-ray and redshift distribution as our main sample—dubbed the non-IR sample (although some of these sources have IRAC detections; see next paragraph). We compare these non-IR AGN plus a sample of 6583 IR-only galaxies with spectroscopic redshifts to our main sample in Section 4. The IR-only galaxies have both a MIPS 24 μm and at least one *Herschel* far-IR detection, but no X-ray detection. For the non-IR AGN, we use the *Herschel* SPIRE 250 μm 5σ limiting flux in the deeper region of the HerMES survey as a generous upper limit on star formation luminosity. Out of the IR-only galaxy sample, 99% of sources have an optical counterpart and 91% have an IRAC detection. We ran IR-only photometric data through SED3FIT and found only 72% (∼5k) of the ∼6.6k galaxies are fitted with an AGN component.

For additional context, we briefly explore the additional two sample populations (6.6k IR-only galaxies and 425 non-IR AGN) in IRAC color–color space in Figure 5 (left). Nearly 40% of the non-IR AGN (small purple dots) and 92% of the IR-only galaxies (gray points) have sufficient (3σ) detections in all four IRAC bands; the same is true for 46% of our main XIR AGN sample (large red dots). In the Donley et al. (2012) IRAC color criteria for identifying luminous AGN ($L_{2-10\rm keV} \geqslant 10^{44}$ erg s^{-1}; wedge outlined by dashed black

―――――――――――
[7] http://vizier.cfa.harvard.edu/
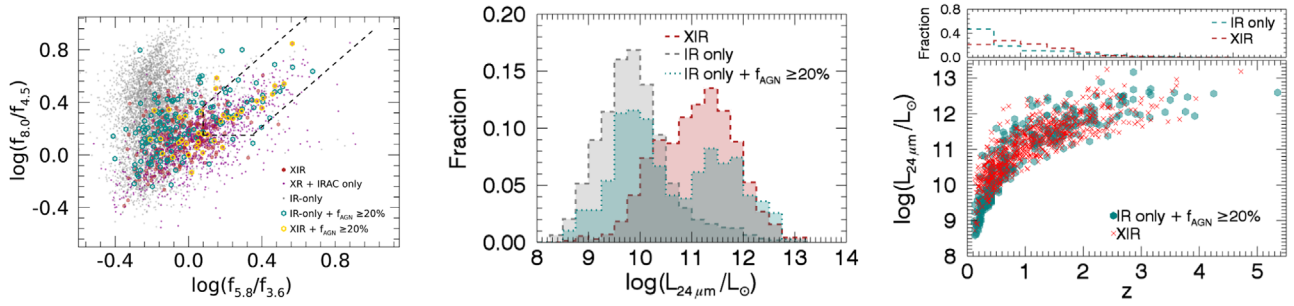
Figure 5. Left: IRAC color–color space used to identify luminous AGN in Donley et al. (2012). Gray points represent the IR-only sources with spec-zs, large red dots mark sources from our main sample of XIR sources, and purple points are additional X-ray sources with IRAC counterparts, but no mid- or far-IR counterparts. The dashed black lines carve out the region belonging to luminous AGN, with minimal contamination from high redshift star-forming galaxies. We note that 15% of the luminous AGN in the IR-only sample also have estimated AGN IR contributions ≥20% (teal circles), while the same is true for 25% of our XIR sample (gold circles). Generally, sources with AGN IR contributions ≥20% are dispersed throughout this IRAC color space, indicating that SED decomposition does not lend itself to luminous AGN identification. Middle: $L_{24\mu m}$ distribution for the 703 X-ray detected sample (red), the 5k IR-only detected sample (gray), and the 389 IR-only sources with ≥20% of IR SED emissions coming from AGN processes (teal). Right: $L_{24\mu m}$ vs. redshift distribution for both the 389 IR-only sample with significant IR AGN contribution (teal) and the X-ray detected sample (red). Top histogram represents the fraction of sources from each sample in redshift bins of size 0.5.

lines), 60 of 327 XIR sources with detections in all four IRAC bands are categorized as luminous AGN with a median $L_{2-10keV} \sim 5.6 \times 10^{43}$ erg s^{-1}; only 23 of the 58 XIR sources with $L_{2-10keV} \geqslant 10^{44}$ erg s^{-1} and IRAC detections are categorized as luminous AGN through the IRAC criteria, which is nearly equivalent to the X-ray luminous AGN recovery rate found in Donley et al. (2012) (38%). This shows that, by using X-ray selection criteria, we are probing a larger population of the most powerful AGN. However, we must note that some powerful AGN are heavily obscured and therefore less X-ray bright (30%–60%, see Section 4.3); we caution readers to consider this selection effect throughout this work.

In the same space, 7% of the non-IR AGN are categorized as luminous AGN with a median $L_{2-10keV} \sim 2.3 \times 10^{44}$ erg s^{-1} and a recovery rate of 32% for all X-ray luminous AGN in the non-IR sample; and out of the 5.6k IR-only sources with spec-zs and sufficient IRAC detections, only 2% ($N = 128$) of sources are deemed luminous AGN (but members of this sample do not have any bona fide X-ray detections, so we cannot determine the recovery rate).

4. Results and Discussion

4.1. Average L_{IR}^{SF} versus Average L_{AGN}

We translate X-ray flux to bolometric AGN luminosity, L_{AGN}, using the equation in Rosario et al. (2012) (R12 hereafter) derived from Maiolino et al. (2007) and Netzer & Trakhtenbrot (2007) for spectroscopically confirmed Type 1 (unobscured) AGN:

$$\log L_{AGN} = \frac{\log L_X - 11.78}{0.721} + 0.845 \qquad (2)$$

where L_X is the 2–10 keV band X-ray luminosity. We average IR contribution from star-forming processes in bins of L_{AGN}, with respect to each redshift interval, and do the same separately for the additional 425 X-ray sources with spectroscopic redshifts but no IR counterparts. We show these results in Figure 6 (left); the dashed line represents the relationship found in Netzer (2009) (N09, hereafter) for local, low luminosity AGN-dominated systems where L_{AGN} is much larger than L_{IR}. Nearly 50% of X-ray-only detected sources fall into the AGN-dominated section, compared to only ∼5% of

individual X-ray and IR detected sources, substantiating the selection of AGN embedded within star-forming galaxies in this analysis and demonstrating the dominance of star formation driven modes in IR luminosities of *Herschel* detected dusty galaxies. This trend is corroborated in several recent works using IR bright X-ray selected AGN (e.g., R12, L17, Dai et al. 2017), indicating that the power-law correlation from N09 is valid when extended to higher luminosities and high-z AGN.

Our low z ($z \lesssim 1$) sample successfully reflects those of other published results with low luminosity AGN ($L_{AGN} < 10^{45}$ erg s^{-1}) showing a flat or uncorrelated relationship between AGN activity and star formation. The higher luminosity AGN in the low z-bins appear to trend in a more positive linear fashion that approaches the N09 relationship. The stronger, positive relationship is most noticeable in the $0.4 < z < 0.8$ bin where the most powerful AGN, while few in number ($N = 6$), are embedded in star-forming galaxies nearly just as bursty as the brightest AGN in the $0.8 < z < 1.2$ bin. These results also appear in L17 and R12, but conflict with the flat, nonexistent relationships found in Stanley et al. (2015) and Dai et al. (2017).

Hickox et al. (2014) and Volonteri et al. (2015) developed models that match similar observational results as those in L17, R12, Chen et al. (2013) and Azadi et al. (2015). In Figure 7, we overlay the Hickox et al. (2014) model curves and see general agreement with the results for our $z \sim 1$ less powerful active galaxies ($L_{AGN} < 10^{45}$ erg s^{-1}), but the model overestimates star-forming luminosity for the more powerful AGN ($L_{AGN} > 10^{45}$ erg s^{-1}) in each redshift range. To create the model, Hickox et al. (2014) generated a sample of galaxies (up to $z = 2$) in which all star-forming galaxies host an AGN during their lifetime, and then incorporated a constant of proportion between SFR and black hole accretion rate (BHAR) over long timescales (log(SFR/BHAR) = 3.6 (Chen et al. 2013; Dai et al. 2017)) and assigned short timescale variabilities in AGN accretion processes (and therefore, luminosity). Generally, the model successfully produces the observed findings when averaging star formation activity in bins of AGN activity, along with the trends observed in the literature when averaging AGN activity in bins of star formation activity, as analyzed in the following section.
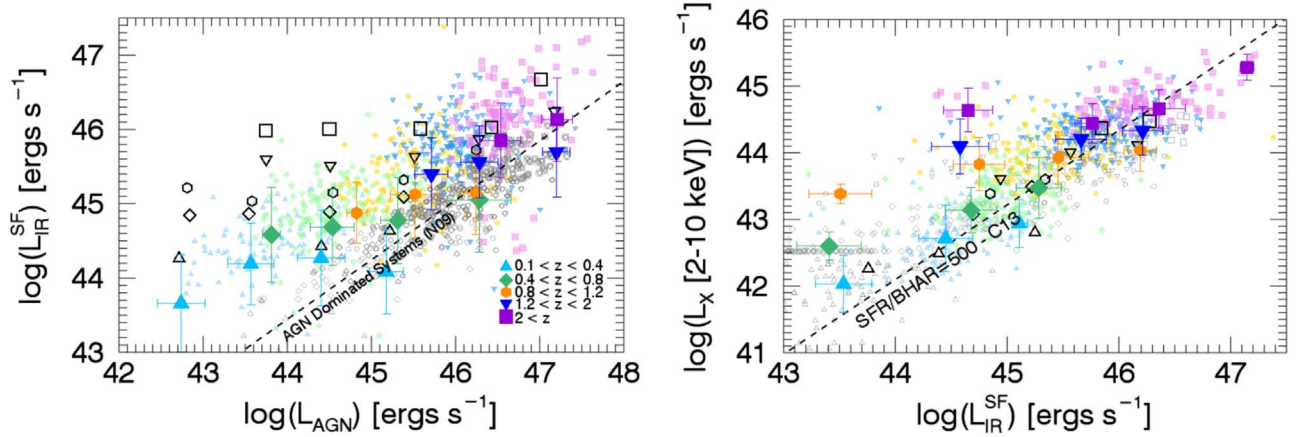
Figure 6. Left: Distribution of AGN bolometric luminosity ($\propto L_X$) vs. L_{IR}^{SF}. The lighter, smaller points are individual AGN. The small, empty gray symbols are X-ray AGN with L_{IR}^{SF} upper limits determined by the HerMES *Herschel* SPIRE 250 μm flux limit. The larger, bolder, filled in points are average $\log(L_{IR}^{SF})$ in bins of $\log(L_{AGN})$, showing both the IR detected (colorful) and IR non-detected (empty gray) X-ray sources. Error bars represent the 1σ dispersion of each bin. Note the star-forming luminosity for the most powerful AGN in the $0.4 < z < 0.8$ z-bin lies directly under the corresponding average star-forming luminosity for the most powerful AGN in the $0.8 < z < 1.2$ z-bin. The black dashed line represents the relationship found in N09 where objects below the line have IR luminosities dominated by AGN activity. Black empty symbols are results from Lanzuisi et al. (2017). Right: Average $\log(L_X)$ in bins of $\log(L_{IR}^{SF})$ compared to results from C13 (Chen et al. 2013). The C13 sample is represented by the black empty shapes. The dashed line is the constant proportional relationship between SFR and BHAR found in C13. Colors, symbols, and error bars are calculated in the same fashion as in the left figure, where the empty gray points denote the IR-only detected sources with an estimated IR AGN fraction $\geqslant 20\%$ with X-ray upper limits defined by the XBoötes survey flux limit.
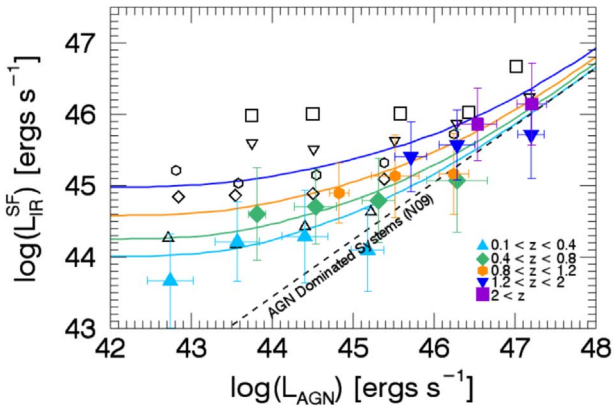
Figure 7. Distribution of AGN bolometric luminosity vs. L_{IR}^{SF} with the black dashed line as defined in Figure 6 (left). The solid lines have colors corresponding to redshift ranges and are the extrapolated trends from the Hickox et al. (2014) simple model incorporating short-term AGN variability, long-term evolving SFRs, and a universal constant of proportion between SFRs and black hole accretion rates.

### 4.2. Average L_X versus Average L_{IR}^{SF}

Recent simulations and observations reveal that AGN accretion (and therefore luminosity) can be highly variable on short timescales—e.g., on the order of 1–2 mag within 0.1–1 Myr (e.g., Di Matteo et al. 2005; Hickox et al. 2014)—whereas star formation processes change at a slower rate over longer timescales. To uncover the relationship between AGN processes and host galaxy SFRs, it might be more appropriate to average AGN activity (the more rapidly changing variable) based on L_{IR}^{SF} (the more stable variable).

Following the analysis in L17 and Chen et al. (2013) (C13, hereafter), we reversed data dependency by averaging $\log(L_X)$ in bins of $\log(L_{IR}^{SF})$. We include 389 IR-only sources with an AGN IR contribution that is $\geqslant 20\%$ of the total IR SED. These IR-only sources have both a MIPS 24 μm and at least one *Herschel* far-IR detection, but no X-ray detection (see Figure 5

for 24 μm population distribution). We take the ratio of IR AGN luminosity to total IR luminosity from the resulting SED and place a cut at $\geqslant 20\%$ to capture the sources with the highest likelihood of hosting an AGN (Ciesla et al. 2015). For these objects, we use the XBoötes survey flux limit as an upper limit for X-ray luminosity. Results are shown in Figure 6 (right) with L17 results overlaid. Error bars represent the 1σ dispersion of the mean X-ray luminosity in each respective bin. The dashed line represents the constant ratio between BHAR (proportional to X-ray luminosity) and SFR found in C13 for 34 X-ray detected AGN at $z = 0.25$–0.8.

We find our results to be in good agreement with the C13 SFR/BHAR ratio. The low z-bins ($z \lesssim 1$) have the strongest positive slope between the same L_{IR}^{SF} intervals studied in C13, which is expected as C13 analyzed data from the same Boötes, *Chandra*, *Herschel*, and *Spitzer* observations used in this paper. While AGN still hover near the SFR/BHAR ratio in the earlier $z > 0.8$ universe, there is no significantly strong upward trend as L_{IR}^{SF} increases for any z-bin, and the nearly $\sim$0.5 dex increase exhibited within the $z > 2$ sample for the highest range of star formation activity has a very small sample size and is therefore unreliable.

Note that these observations are limited to the depths of the 24 μm survey; an object at $z \sim 1$ with a 24 μm luminosity of $L_{24\mu m} = 10^{44}$ erg s^{-1} is pushing the survey observational limits and might be undetected. This means that the weakest star formation bins in this analysis may be lacking contributions from some fainter, intermediate redshift galaxies and AGN. Conversely, some powerful AGN are heavily obscured by high column densities of dust and gas. In fact, studies have shown that 90% galaxies with high 24 μm to optical flux ratios have IR and X-ray signatures indicating the presence of heavily obscured AGN (Fiore et al. 2008; Treister et al. 2009). These AGN are expected to have intrinsic X-ray luminosities in excess of 10^{44} erg s^{-1}, at $z \sim 1$–2, which could drive the more star-forming L_{IR}^{SF} bins further upward and into stronger agreement with the C13 trend.
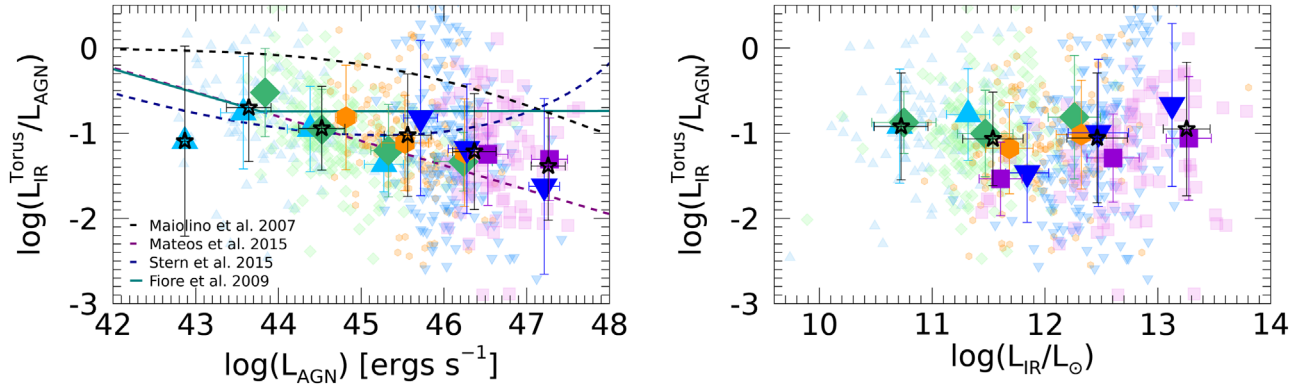
Figure 8. Left: CF vs. bolometric AGN luminosity. Averages for the X-ray detected sample are computed in bins of L_{AGN} and in respective redshift ranges. We also computed averages for the entire sample, irrespective of redshift range, as indicated by the empty black stars. The black dashed line represents the fraction of obscured AGN as a function of bolometric AGN luminosity found by Maiolino et al. (2007). The purple dashed line, navy dashed line, and turquoise solid line correspond to mid-IR/L_{AGN} fractions found by translating the X-ray to 6 μm relationships derived in Mateos et al. (2015), Stern (2015), and Fiore et al. (2009), respectively. Right: CF vs. total IR luminosity. Averages, colors, and symbols are derived in the same fashion as those in the figure to the left.
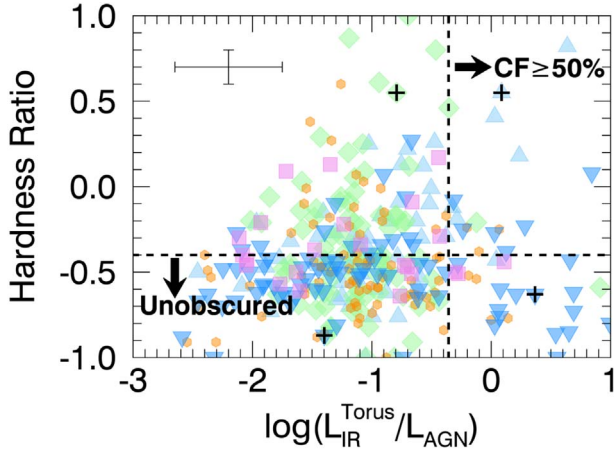
Figure 9. CF vs. HR for the 330 XIR AGN with sufficient X-ray counts to determine HRs. Colors and shapes are the same as those in Figure 6. Average error bars are presented in the top left corner. To the right of the black dashed vertical line lies AGN with CFs greater than 50%. Below the black dashed horizontal line lies AGN with HRs indicative of unobscured cores. SEDs for sources marked with crosses are in the Appendix, providing examples of some of the more extreme and contradictory AGN in this sample.

The observed differences in correlation between the two averaging methods are likely due to the inherent rate of variation between the two physical processes, with star formation being the more stable measurement and AGN accretion being the more variable measurement. These differences in correlation methods were also confirmed by Dai et al. (2017) for similar samples of X-ray selected AGN. Lapi et al. (2014) found similar results when exploring the observational phenomenon of the co-evolutionary relationship between AGN and host galaxies at high redshifts ($z \gtrsim 1.5$) using a semi-analytical model. Combining observational data on AGN in star-forming galaxies with high-z AGN luminosity functions and host galaxy stellar luminosity functions, the model shows galaxy SFRs that remain relatively constant over a long period of time then suddenly undergo a rapid decrease in star formation when the SMBH is triggered into an active phase. The model also predicts that as the SMBH grows, a fraction of the cold interstellar gas and dust within the spiral arms of a galaxy is drawn toward the nucleus to help form and grow the dusty torus. The AGN will feed off this reservoir and the most powerful AGN will have feedback processes that strip away some of the remaining cold gas and dust, further suppressing star formation processes and eventually slowing its own growth as well. Observations at various epochs within the model easily reproduce both of the trends shown in Figure 6, and when combined with the publications and findings discussed in Section 4.1, indicate that a more detailed study on the relationship between short-term AGN variability and host galaxy cold gas and dust properties is necessary to arrive at any definitive conclusions.

4.3. Dust CFs

We can determine how dust obscured an accreting SMBH is by assessing the relationship between how much high energy radiation from accretion disk processes is observed (which therefore escapes the dusty torus), versus how much radiation is detected from the dusty torus itself. A commonly used dust CF proxy is the ratio of dusty torus emission, L_{Tor} (which dominates in the mid- to far-IR), to bolometric AGN luminosity, L_{AGN} (e.g., Maiolino et al. 2007; Treister et al. 2008; Rowan-Robinson et al. 2009). To compute the dust CF for our sample, we use the bolometric AGN luminosities derived from Equation (2), and derive L_{Tor} from the dusty torus components in each source's respective AGN SED (i.e., we remove the IR emission originating solely from the accretion disk from each AGN SED template for each source and keep only the dusty torus emission components). We caution that systematics from the fixed CF (75%) in the AGN SEDs may produce biased estimates of dusty torus emission in this analysis (see Section 3).

We note that this proxy (CF = L_{Tor}/L_{AGN}) is used under the assumption that accretion disk emission and the resulting dusty torus emission are generally isotropic. However, the work of Stalevski et al. (2016) shows that, when considering the anisotropy of these emission processes for Type 1 AGN with $L_{AGN} \sim 10^{45}$ erg s^{-1}, this proxy can underestimate intrinsically low CFs and overestimate high CFs, while for Type 2 AGN of similar luminosities, this proxy always underestimates the true CF. We assess the impact of this assumption on our results at the end of this section.
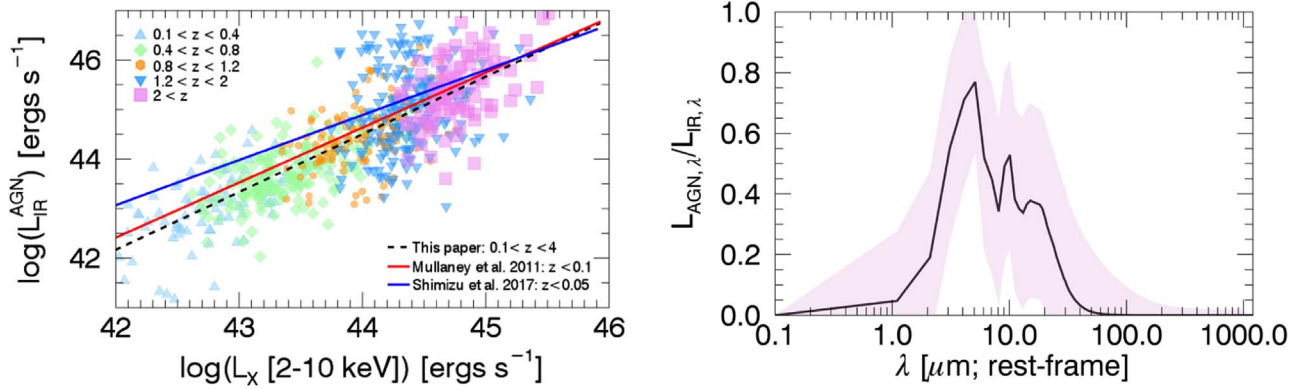
Figure 10. Left: IR AGN luminosity as a function of L_X for the X-ray AGN. The black dashed line represents the linear relationship found in log space between the two AGN luminosities. The red and blue lines represent the relationship determined from generated average SEDs for local AGN by Mullaney et al. (2011) and Shimizu et al. (2017), respectively. Right: Composite f_{AGN} as a function of rest-frame wavelength using all 703 X-ray selected AGN. The black line is the median value at all wavelengths in bins of $\Delta\lambda = 1\ \mu$m and the 1σ scatter for each $\Delta\lambda$ is indicated by the shaded pink region.
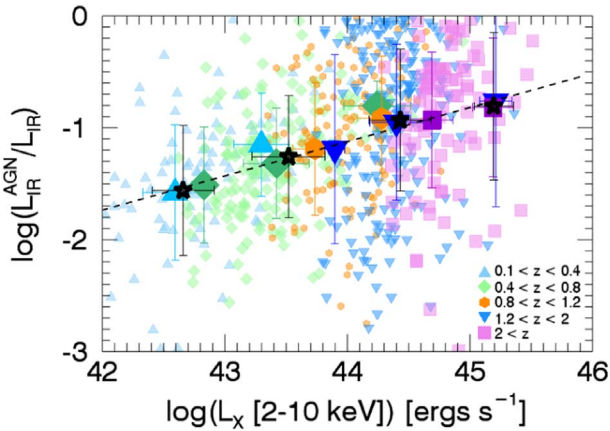
Figure 11. AGN fractions for the X-ray detected sample as a function of X-ray luminosity. Averages are computed in bins of L_X, respective of redshift range, with error bars representing the 1σ dispersion of the mean. Black empty stars represent the averages across X-ray luminosity, regardless of age in the universe.

The average dust CF decreases with an increase in AGN activity for our X-ray detected AGN sample (Figure 8, left). This trend correlates nicely with the luminosity-dependent AGN unified model where dust CF is anti-correlated with bolometric luminosity, also known as the *receding torus model* (Lawrence 1991). Taking the model implications a step further, it follows that the average CF within a sample of AGN corresponds directly to the fraction of Type 2 (obscured) AGN. In this work, we find an average CF of 33% for the X-ray detected AGN. This average CF is similar but slightly lower than those found in the literature: Rowan-Robinson et al. (2009) used *Chandra* and/or *Spitzer* data to determine CFs for 658 AGN and found an average dust CF of 40%; Mateos et al. (2015) determined a spectroscopically confirmed Type 2 fraction of 43% on a sample of 250 X-ray selected AGN with dust CFs ranging from 20%–50% when averaged in bins of X-ray luminosity; Lanzuisi et al. (2009) found a higher Type 2 fraction at 55% of mid-IR bright X-ray selected AGN, and Hickox et al. (2007) selected IR AGN in the same field as this study and used spectroscopic and optical to mid-IR color distributions to determine a Type 2 fraction of 43%. The

observed luminosity dependence agrees most with the trend found in Mateos et al. (2015) (shown as the purple dashed line in Figure 8, left), who also used multicomponent SEDs to determine the AGN contribution to mid-IR luminosity. A newer study by Mateos et al. (2017) investigated the lack of one to one correlation between Type 2 fraction and average CF for their complete sample of optically classified X-ray AGN. They identify a missing population of X-ray obscured AGN, and when the high CFs of these obscured AGN are accounted for, the population CF average grows to nearly 60% with a less significant luminosity-dependent relationship. It is possible that the CFs of heavily obscured AGN in the Boötes region would effectively raise the average CF across all redshift ranges and AGN luminosities to a similar value, but that analysis is beyond the scope of this work.

In Figure 8, right, we find an overall flat relationship between total IR luminosity and CFs for the X-ray selected sample, hovering at an average of ∼10% across all luminosities. While there appears to be some positive relationship for all redshift bins $z > 0.4$ starting at $\log(L_{IR}/L_\odot) \approx 11.5$, the sample dispersion is large, spanning $\pm\sim50\%$ (or more) for each average data point within each redshift bin. Therefore, any observed positive correlation is weak and would require further investigation for verification.

We also recover trends that challenge the inclination-based unified model: there is no clear bimodal distribution for CFs in the XIR AGN population; instead we see a distribution of CFs that cover the entire possible range at significant percentages. To investigate, we further restrict our sample to the 330 XIR AGN with sufficient X-ray counts to determine hardness ratios (HRs; i.e., H−S/H+S, an indicator of AGN obscuration; e.g., Green et al. 2004) and find the majority (∼57%) are unobscured with corresponding HRs $\lesssim -0.5$ and an overall wide spread in CFs averaging 35% ± 1.03% (see Figure 9). Concentrating only on the 187 XIR AGN with unobscured HRs, we find 11% have CFs $\gtrsim 50\%$, indicating that a defining CF cutoff limit between Type 1 and Type 2 AGN based on X-ray absorption is nonexistent. Mateos et al. (2016) found similar results using 227 spectroscopically confirmed and categorized X-ray AGN; while the different types of AGN had clearly different CF distributions (with type 2(1) peaking at high(low) CFs), there was still a very strong overlap in CF distributions; roughly 20% of Type 1 AGN had CFs > 0.5 and
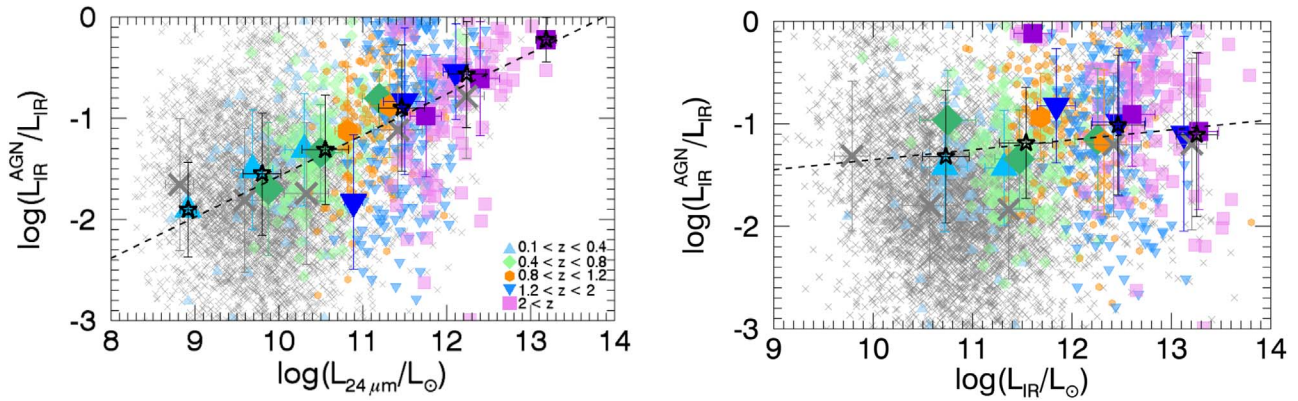
Figure 12. These two figures represent the ratio of IR AGN luminosity to host galaxy total IR luminosity (i.e., AGN fraction) as a function of host galaxy luminosities. Colors and symbols are the same as those in Figure 8, with gray x's denoting the individual ∼6k IR-only galaxies as defined in Section 3 and their averages in luminosity buckets of size 1 dex are represented as large gray x's. Left: The logarithm of the AGN fraction as a function of 24 μm luminosity. The XIR sample shows a clear, but weak, correlation between 24 μm luminosity and AGN fractions. Right: The logarithm of the AGN fraction as a function of total IR luminosity, following the same legend as that in the figure on the left. There appears to be no clear relationship between total IR luminosity and AGN fraction, indicating a need for individual IR SED decomposition when estimating AGN fractions across IR luminosity space.

40% of Type 2 AGN had CFs < 0.5. Merloni et al. (2014) used optical photometry and/or spectra paired with hard X-ray data for ∼1300 AGN and found 31% of the entire sample sits in a similar contradictory region where optical signatures point toward an unobscured nucleus while X-ray data indicates considerable gas and dust absorption, or vice versa with optical evidence for an obscured nuclear region and no absorption of soft X-rays. This work and the aforementioned suggest that Type 1 and Type 2 AGN may not be observationally distinct due to the line-of-sight inclination of the dusty torus but instead due to other physical accretion-related mechanisms.

Recently, Ricci et al. (2017) showed that the relationship between AGN luminosity and CF flattens out when dividing X-ray AGN into separate bins of Eddington ratios (λ_E; mass-normalized BHAR), indicating that the AGN line-of-sight obscuration is not the universal driver of CF distributions. Instead, λ_E and CF maintain a steady positive correlation up until the sublimating Eddington limit for dusty gas particles, in which the CF sharply declines. These results point toward strength in radiation pressure from accretion activities being the main regulator of observed obscuration fractions, and that Type 1 and Type 2 AGN are actually physically different objects (as categorized by λ_E) that could be better unified within the context of black hole growth over time. Exploration of this relationship is beyond the scope of this analysis; we refer readers to Beckmann et al. (2009), Winter et al. (2009), Ezhikode et al. (2016), Lusso et al. (2012), Lawrence & Elvis (2010), and Mateos et al. (2017) for further discussions that precede the Ricci et al. (2017) results.

We explored how the Stalevski et al. (2016) equation and coefficients (see their Equation (8) and Table 1) for correcting isotropically assumed dust CFs affect our results by first identifying Type 1 and Type 2 AGN using the inclination angles used in the SED fitting procedure. The AGN SED fitting model used in this paper includes two possible nuclear line-of-sight angles: 0° (face-on aka Type 1 unobscured nucleus) or 90° (edge-on aka Type 2 nucleus viewed through the disk). Based on this criteria, 61% of our XIR sources are categorized as Type 1 AGN, and the remainder are categorized as Type 2 AGN, which is consistent with the average CF derived earlier in this section. Interestingly, the majority of Type 2 AGN in this sample (77%) have CFs below ⩽10%, while Type 1 AGN

exhibit no general CF preference. Both AGN types have median AGN luminosities of $L_{AGN} \sim 3 \times 10^{45}$ erg s^{-1}.

We applied each set of coefficients corresponding to the three reported example optical depths ($\tau_{9.7\mu m} = 3, 5, 10$ in Stalevski et al. 2016) to the respective AGN types. The overall effect is strongest for AGN (of both types) with originally estimated CFs less than 20%, which is nearly three-quarters of the 703 AGN; for each set of coefficients, dust CFs were increased to ⩾20%, due to the lower limits assumed in Stalevski et al. (2016), with the average individual differences being +33% to the respective CFs. This effectively flattens out any trends seen in Figure 8, where the original average CF of 33% is now a corrected average CF of 49%. It is worth noting that these equations were originally derived for a luminous AGN with $L_{AGN} \sim 10^{45}$ erg s^{-1}; a third of our sample at lower AGN luminosities sees an average CF correction of ∼+25%, while the remaining more powerful population has a 10% higher average CF correction than that of the low luminosity AGN. Thus, due to the the underlying assumptions in CFs and the wide range in AGN luminosities probed in this work, we are unfortunately limited from making any further interpretations.

4.4. AGN Contribution in the IR

The wide IR coverage in the Boötes region when paired with the multicomponent SED fitting model SED3FIT is advantageous in effectively constraining intrinsic IR AGN luminosities across a broad redshift range. This is useful to avoid situations of overestimating host galaxy properties (e.g., SFRs) in cases with little IR photometry and/or possible indications of AGN activity. In the following, we explore the extracted IR AGN luminosities in the 8–1000 μm range (L_{AGN}^{IR}, hereafter) as a function of L_X, as well as the fraction of total IR luminosity attributed to AGN emissions (L_{AGN}^{IR}/L_{IR} or f_{AGN}, hereafter) as a function of L_X, L_{IR}, and $L_{24\mu m}$.

There is a strong correlation between X-ray activity and total IR AGN luminosity within our X-ray detected sample. This relationship is similar to the driving trend determined in Mullaney et al. (2011), even though a large portion of our sample contains galaxies with low AGN fractions ($f_{AGN} < 10\%$) out to high redshifts. Mullaney et al. (2011) modeled
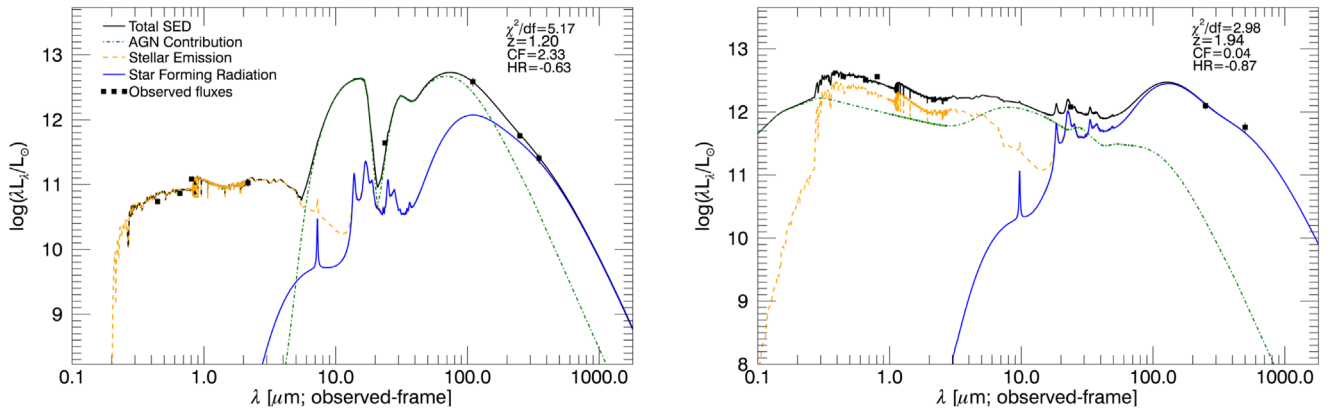
Figure 13. Generated example "extreme" SEDs of AGN with HRs $\lesssim -0.5$, indicative of an unobscured nucleus with with little to no obscuring dust and gas. Left: SED of an X-ray unobscured AGN with high CF. Right: SED of an X-ray unobscured AGN with a low CF.

intrinsic IR AGN SEDs for only 11 local ($z < 0.1$) AGN with polycyclic aromatic hydrocarbon emission lines indicative of IR luminosities dominated by AGN ($f_{AGN} > 90\%$). As seen in Figure 10 (left), we derive a nearly equivalent relationship for AGN spanning a much larger redshift and AGN fraction range, suggesting that this relationship is universal. The black dashed line denotes our sample relationship, where

$$\log\left(\frac{L_{IR}^{AGN}}{10^{43}\ \text{erg s}^{-1}}\right) = (0.33 \pm 0.06)$$
$$+ (1.16 \pm 0.05)\log\left(\frac{L_X}{10^{43}\ \text{erg s}^{-1}}\right) \quad (3)$$

with a strong, positive correlation coefficient of 0.78. The red line denotes the slope found in Mullaney et al. (2011) (1.11 ± 0.07) and the blue line denotes the slightly weaker relationship found by Shimizu et al. (2017) (0.91 ± 0.06) who analyzed a sample of 313 local X-ray selected AGN with *Herschel* and *WISE* detections; additionally, Kirkpatrick et al. (2017) found a more extreme relationship (3.76 ± 0.08, not plotted) for 53 $z \sim 1$–2 composite galaxies in the GOODS-S field with *Spitzer* and *Herschel* detections. Our work provides the first $0.1 < z < 4$ pure AGN IR SED relationship estimated using a statistically significant population size, providing future studies the ability to estimate the total IR emission of a high-z AGN using only X-ray data. A deeper X-ray study with a similar amount multiwavelength IR data and de-absorbed X-ray luminosities would be needed to confirm this relationship is complete to lower luminosity X-ray AGN at $z > 0.1$.

The median IR AGN contribution across all sources is 8%–30%, indicating that roughly 70%–90% of IR light from this set of galaxies is coming from star formation processes. When restricting our sample to the 337 ULIRGs ($L_{IR} > 10^{12}\ L_\odot$), we find a median $f_{AGN} = 13\%$, similar to the fraction found in Nardini et al. (2008) for local ULIRGs. Looking at the median composite, rest-frame f_{AGN} as a function of wavelength in Figure 10 (right), we find that AGN contribution heavily affects the mid-IR, with a maximum of nearly 80% at 5–6 μm. While the impact of AGN contribution trails off at wavelengths greater than $\sim$30 μm in Figure 10 (similar to other results, e.g., Mullaney et al. 2011; Kirkpatrick et al. 2012), the f_{AGN} sample distribution is broad at each wavelength with an average scatter of $\pm$20%–30%, implying that multicomponent SED analysis is

crucial in accurately determining the true AGN contribution for individual sources, particularly for cases without X-ray observations to constrain L_{AGN}^{IR}.

On average, f_{AGN} increases with increasing X-ray and 24 μm luminosity, but not with total IR luminosity (see Figures 11 and 12). The latter tells us that any trends found with L_{AGN}^{IR} are not driven simply by the host galaxy's luminosity; or, in other words, a broad range of IR AGN fractions can be found embedded in variously luminous galaxies. As expected, for the IR-only galaxies (represented by gray x's) we see fairly low AGN fractions at low and average luminosities; yet, at higher luminosities, the IR-only galaxies and XIR AGN appear similar across the $\log(f_{AGN})$–$\log(L_{24\mu m})$ relationship (possibly due to incomplete sample selection effects and/or SED modeling degeneracies in high-redshift submillimeter galaxies, e.g., da Cunha et al. 2015). The 128 IR-only galaxies with IRAC colors indicative of embedded luminous AGN (not highlighted; see Section 3 for sample definition) span a similar range of 24 μm luminosities and follow nearly exactly the same trends as the XIR sample. We also considered the relationship between f_{AGN} and host galaxy stellar mass; again, we find a flat, nonexistent correlation. We note that this sample occupies a host galaxy stellar mass distribution similar to those found in the literature for AGN host galaxies, with a mean stellar mass of $\log(M_*) = 10.83 \pm 0.58$ (e.g., Hickox et al. 2009; Xue et al. 2010).

We determine a clear but weak relationship in $\log(f_{AGN})$–$\log(L_{24\mu m})$ and in $\log(f_{AGN})$–$\log(L_X)$, both with slopes $\approx$0.11. Both correlations have large intrinsic scatters and weak correlation coefficients at $\sim\pm$60% and $\sim$0.36, respectively. Ciesla et al. (2015) shows that f_{AGN} predictions below 20% are accompanied with large uncertainties and therefore should be disregarded; these uncertainties vary across AGN types and it is unclear how they might vary across AGN luminosities. To investigate whether there is a stronger relationship present in our more certain f_{AGN} calculations, we restrict our sample to $f_{AGN} \geqslant 20\%$, which is about 28% of the entire sample with an average $\log(L_{24\mu m}) = 11.56 \pm 0.66$ and $\log(L_X) = 44.30 \pm 0.54$. Instead, we find an even weaker slope at $\sim$0.06 with a correlation coefficient of $\sim$0.12 for both sample populations, and again a large range of values. These results directly indicate a need for individual SED decomposition to infer the fraction of IR output attributed by an AGN.
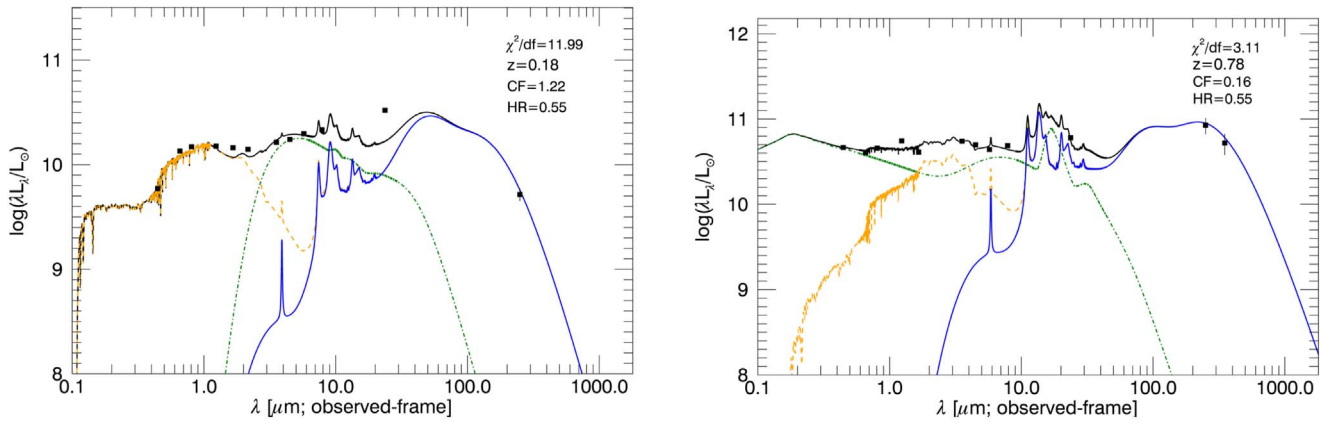
Figure 14. Generated example extreme SEDs of AGN with HRs $\gtrsim 0.5$, indicative of an obscured nucleus with thick absorbing circumnuclear gas and dust. Left: SED of an X-ray obscured AGN with a high CF. Right: SED of an X-ray obscured AGN with a low CF.

5. Summary and Conclusions

We explored the relationship between AGN activity and host galaxy dust properties across the tail end of peak AGN and galaxy growth in the universe (redshifts $0.2 < z < 5$) using *Chandra*, *Herschel*, *Spitzer*, and NOAO Telescope observations in the Boötes field. We successfully disentangled AGN and star formation radiative processes in the IR spectrum for 703 IR bright X-ray AGN, using multicomponent SED fitting code, SED3FIT (Berta et al. 2013), and determined the AGN-corrected integrated rest-frame IR luminosity attributed to star formation, total IR AGN luminosity, AGN dust CFs, and AGN fractions. Our main results can be summarized as follows:

1. We find flat trends consistent with the literature when averaging L_{IR}^{SF} in bins of bolometric AGN luminosity for less powerful AGN ($L_{AGN} < 10^{45} \, \mathrm{erg \, s^{-1}}$), as well as the stronger correlations found when averaging L_X in bins of star formation activity for AGN at low redshifts ($0.1 < z < 0.8$).
2. We further decompose AGN SEDs to isolate the dusty torus component in the IR and compare to the bolometric AGN luminosity to estimate nuclear obscuration. We determine an average dust CF slightly lower than that found in the literature at CF = 33%, which indicates a Type 2 (obscured) population of roughly a third. Further investigation of X-ray hardness reveals several X-ray AGN with CFs that contradict the expected nuclear obscuration determined by HRs (e.g., high CF with a low HR that is indicative of an unobscured central engine), providing further evidence that observational differences between AGN types are not primarily driven by line-of-sight dusty torus inclination.
3. We uncover a wide range in the fraction of IR luminosity attributed to AGN activity across all redshifts, and determine no statistically significant trend exists when evaluating f_{AGN} as a function of total IR, X-ray, or 24 μm luminosity. The mean f_{AGN} as a function of rest-frame IR wavelength shows peak AGN contamination lives in the mid-IR range and becomes insignificant at wavelengths larger than $\sim 30 \, \mu$m, but the sample dispersion is large ($\pm 20\%$–30%) at all wavelengths. These results demonstrate the importance of SED decomposition for individual AGN and host galaxies in order to accurately quantify AGN contamination in the IR, particularly prior to using IR photometry to estimate host galaxy properties.
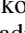
While considering all of the implications discussed in this paper, we should remember that current far-IR detections of intermediate and high redshift X-ray AGN in star-forming galaxies are limited by the sensitivity of far-IR and sub-millimeter observatories like the *Herschel Space Observatory*. The currently available resolutions limit us to the most powerful star-forming systems and we need deeper, more sensitive observations to capture the dust properties of AGN that reside in smaller and/or quiescent galaxies in order to complete the evolutionary picture.

Appendix
Sample Extreme SEDs

We provide sample SEDs of AGN that reside in the more extreme regions shown in Figure 9, marked by black crosses. Figure 13 shows two objects with X-ray HRs indicative of an unobscured nucleus with little to no dust or gas absorbing their X-ray luminosities. However, the object on the left has a high dusty torus CF, which is contradictory to what we would expect to see based on the HR and the inclination-based AGN unification model (Antonucci 1993; Urry & Padovani 1995). Similarly, in Figure 14 we see two objects with HRs that signify the presence of highly obscuring column densities, but SED decomposition for the object on the right determined a low CF that contradicts the HR estimate. These objects support the need for a different perspective on what truly drives the observational differences between AGN classifications.

ORCID iDs

Arianna Brown ⬤ https://orcid.org/0000-0002-7530-8857
Hooshang Nayyeri ⬤ https://orcid.org/0000-0001-8242-9983
Jingzhe Ma ⬤ https://orcid.org/0000-0003-4178-0800
Ryan C. Hickox ⬤ https://orcid.org/0000-0003-1468-9526
Mojegan Azadi ⬤ https://orcid.org/0000-0001-6004-9728

References

Aird, J., Coil, A. L., Moustakas, J., et al. 2012, ApJ, 746, 90
Aird, J., Nandra, K., Laird, E. S., et al. 2010, MNRAS, 401, 2531
Alexander, D. M., Bauer, F. E., Brandt, W. N., et al. 2003, AJ, 125, 383
Alexander, D. M., & Hickox, R. C. 2012, NewAR, 56, 93
Antonucci, R. 1993, ARA&A, 31, 473
Ashby, M. L. N., Stern, D., Brodwin, M., et al. 2009, ApJ, 701, 428
Azadi, M., Aird, J., Coil, A. L., et al. 2015, ApJ, 806, 187
Azadi, M., Coil, A. L., Aird, J., et al. 2017, ApJ, 835, 27
Barmby, P., Alonso-Herrero, A., Donley, J. L., et al. 2006, ApJ, 642, 126
Beckmann, V., Soldi, S., Ricci, C., et al. 2009, A&A, 505, 417
Berta, S., Lutz, D., Santini, P., et al. 2013, A&A, 551, A100
Bianchi, S., Maiolino, R., & Risaliti, G. 2012, AdAst, 2012, 782030
Blandford, R. D., & Payne, D. G. 1982, MNRAS, 199, 883
Bonfield, D. G., Jarvis, M. J., Hardcastle, M. J., et al. 2011, MNRAS, 416, 13
Brand, K., Brown, M. J., Dey, A., et al. 2006, ApJ, 641, 140
Brandt, W. N., & Alexander, D. M. 2015, A&ARv, 23, 1
Brusa, M., Civano, F., Comastri, A., et al. 2010, ApJ, 716, 348
Casey, C. M., Narayanan, D., & Cooray, A. 2014, PhR, 541, 45
Chen, C.-T. J., Hickox, R. C., Alberts, S., et al. 2013, ApJ, 773, 3
Chen, C.-T. J., Hickox, R. C., Alberts, S., et al. 2015, ApJ, 802, 50
Ciesla, L., Charmandaris, V., Georgakakis, A., et al. 2015, A&A, 576, A10
Civano, F., Marchesi, S., Comastri, A., et al. 2016, ApJ, 819, 62
Condon, J. J., Anderson, E., & Broderick, J. J. 1995, AJ, 109, 2318
Cowley, M. J., Spitler, L. R., Tran, K.-V. H., et al. 2016, MNRAS, 457, 629
Croton, D. J., Springel, V., White, S. D. M., et al. 2006, MNRAS, 365, 11
da Cunha, E., Charlot, S., & Elbaz, D. 2008, MNRAS, 388, 1595
da Cunha, E., Walter, F., Smail, I. R., et al. 2015, ApJ, 806, 110
Daddi, E., Alexander, D. M., Dickinson, M., et al. 2007, ApJ, 670, 173
Dai, Y. S., Wilkes, B. J., Bergeron, J., et al. 2017, MNRAS, 478, 4238
Davies, R. I., Burtscher, L., Rosario, D., et al. 2015, ApJ, 806, 127
Dekel, A., Birnboim, Y., Engel, G., et al. 2009, Natur, 457, 451
Del Moro, A., Alexander, D. M., Mullaney, J. R., et al. 2013, A&A, 549, A59
Delvecchio, I., Lutz, D., Berta, S., et al. 2015, MNRAS, 449, 373
Di Matteo, T., Springel, V., & Hernquist, L. 2005, Natur, 433, 604
Diamond-Stanic, A. M., Moustakas, J., Tremonti, C. A., et al. 2012, ApJL, 755, L26
Dijkstra, M., & Loeb, A. 2009, MNRAS, 400, 1109
Donley, J. L., Koekemoer, A. M., Brusa, M., et al. 2012, ApJ, 748, 142
Donley, J. L., Rieke, G. H., Rigby, J. R., & Pérez-González, P. G. 2005, ApJ, 634, 169
Ellison, S. L., Mendel, J. T., Patton, D. R., & Scudder, J. M. 2013, MNRAS, 435, 3627
Ellison, S. L., Teimoorinia, H., Rosario, D. J., & Mendel, J. T. 2016, MNRAS, 458, L34
Ezhikode, S. H., Gandhi, P., Done, C., et al. 2016, MNRAS, 472, 3492
Fabian, A. C. 2012, ARA&A, 50, 455
Fazio, G. G., Hora, J. L., Allen, L. E., et al. 2004, ApJS, 154, 10
Ferrarese, L., & Merritt, D. 2000, ApJL, 539, L9
Fiore, F., Grazian, A., Santini, P., et al. 2008, ApJ, 672, 94
Fiore, F., Puccetti, S., Brusa, M., et al. 2009, ApJ, 693, 447
Fritz, J., Franceschini, A., & Hatziminaoglou, E. 2006, MNRAS, 366, 767
Gabor, J. M., & Bournaud, F. 2014, MNRAS, 441, 1615
Geach, J. E., Hickox, R. C., Diamond-Stanic, A. M., et al. 2014, Natur, 516, 68
Gonzalez, A. H., Brodwin, M., Brown, M. J. I., et al. 2010, AAS Meeting, 216, 415.13
Goulding, A. D., Alexander, D. M., Bauer, F. E., et al. 2012, ApJ, 755, 5
Green, P. J., Silverman, J. D., Cameron, R. A., et al. 2004, ApJS, 150, 43
Griffin, M. J., Abergel, A., Abreu, A., et al. 2010, A&A, 518, L3
Gültekin, K., Richstone, D. O., Gebhardt, K., et al. 2009, ApJ, 698, 198
Haardt, F., & Maraschi, L. 1991, ApJL, 380, L51
Haas, M., Klaas, U., Müller, S. A. H., et al. 2003, A&A, 402, 87
Harrison, C. M., Alexander, D. M., Mullaney, J. R., & Swinbank, A. M. 2014, MNRAS, 441, 3306

Hickox, R. C., & Alexander, D. M. 2018, ARA&A, 56, 625
Hickox, R. C., Jones, C., Forman, W. R., et al. 2007, ApJ, 671, 1365
Hickox, R. C., Jones, C., Forman, W. R., et al. 2009, ApJ, 696, 891
Hickox, R. C., Mullaney, J. R., Alexander, D. M., et al. 2014, ApJ, 782, 9
Ho, L. C. 2008, ARA&A, 46, 475
Hopkins, P. F., Hayward, C. C., Narayanan, D., & Hernquist, L. 2012, MNRAS, 420, 320
Hopkins, P. F., & Hernquist, L. 2009, ApJ, 694, 599
Hopkins, P. F., Hernquist, L., Cox, T. J., et al. 2006, ApJS, 163, 1
Jannuzi, B. T., & Dey, A. 1999, in ASP Conf. Ser. 191, Photometric Redshifts and the Detection of High Redshift Galaxies, ed. R. Weymann et al. (San Francisco, CA: ASP), 111
Jorstad, S. G., Marscher, A. P., Lister, M. L., et al. 2005, AJ, 130, 1418
Kauffmann, G., & Haehnelt, M. 2000, MNRAS, 311, 576
Kenter, A., Murray, S. S., Forman, W. R., et al. 2005, ApJS, 161, 9
Kirkpatrick, A., Alberts, S., Pope, A., et al. 2017, ApJ, 849, 111
Kirkpatrick, A., Pope, A., Alexander, D. M., et al. 2012, ApJ, 759, 139
Kochanek, C. S., Eisenstein, D. J., Cool, R. J., et al. 2012, ApJS, 200, 8
Kormendy, J., & Ho, L. C. 2013, ARA&A, 51, 511
Kormendy, J., & Richstone, D. 1995, ARA&A, 33, 581
Lanzuisi, G., Delvecchio, I., Berta, S., et al. 2017, A&A, 602, A123
Lanzuisi, G., Piconcelli, E., Fiore, F., et al. 2009, A&A, 498, 67
Lanzuisi, G., Ranalli, P., Georgantopoulos, I., et al. 2015, A&A, 573, A137
Lapi, A., Raimundo, S., Aversa, R., et al. 2014, ApJ, 782, 69
Lawrence, A. 1991, MNRAS, 252, 586
Lawrence, A., & Elvis, M. 2010, ApJ, 714, 561
Lehmer, B. D., Alexander, D. M., Bauer, F. E., et al. 2010, ApJ, 724, 559
Leung, G. C. K., Coil, A. L., Azadi, M., et al. 2017, ApJ, 849, 48
Lusso, E., Comastri, A., Simmons, B. D., et al. 2012, MNRAS, 425, 623
Lutz, D., Sturm, E., Tacconi, L. J., et al. 2008, ApJ, 684, 853
Magorrian, J., Tremaine, S., Richstone, D., et al. 1998, AJ, 115, 2285
Maiolino, R., Shemmer, O., Imanishi, M., et al. 2007, A&A, 468, 979
Marconi, A., & Hunt, L. K. 2003, ApJL, 589, L21
Mateos, S., Carrera, F. J., Alonso-Herrero, A., et al. 2015, MNRAS, 449, 1422
Mateos, S., Carrera, F. J., Alonso-Herrero, A., et al. 2016, ApJ, 819, 166
Mateos, S., Carrera, F. J., Barcons, X., et al. 2017, ApJL, 841, L18
Mendez, A. J., Coil, A. L., Aird, J., et al. 2013, ApJ, 770, 40
Merloni, A., Bongiorno, A., Brusa, M., et al. 2014, MNRAS, 437, 3550
Miley, G. 1980, ARA&A, 18, 165
Mineo, S., Gilfanov, M., & Sunyaev, R. 2012a, MNRAS, 419, 2095
Mineo, S., Gilfanov, M., & Sunyaev, R. 2012b, MNRAS, 426, 1870
Mullaney, J. R., Alexander, D. M., Aird, J., et al. 2015, MNRAS, 453, L83
Mullaney, J. R., Alexander, D. M., Goulding, A. D., & Hickox, R. C. 2011, MNRAS, 414, 1082
Mullaney, J. R., Pannella, M., Daddi, E., et al. 2012, MNRAS, 419, 95
Murray, S. S., Kenter, A., Forman, W. R., et al. 2005, ApJS, 161, 1
Mushotzky, R. 2004, in Supermassive Black Holes in the Distant Universe, ed. A. J. Barger (Dordrecht: Springer Netherlands), 53
Nandra, K., & Pounds, K. A. 1994, MNRAS, 268, 405
Nardini, E., Risaliti, G., Salvati, M., et al. 2008, MNRAS, 385, L130
Nenkova, M., Sirocky, M. M., Ivezić, Ž., & Elitzur, M. 2008a, ApJ, 685, 147
Nenkova, M., Sirocky, M. M., Nikutta, R., Ivezić, Ž., & Elitzur, M. 2008b, ApJ, 685, 160
Netzer, H. 2009, MNRAS, 399, 1907
Netzer, H. 2015, ARA&A, 53, 365
Netzer, H., & Trakhtenbrot, B. 2007, ApJ, 654, 754
Oliver, S. J., Bock, J., Altieri, B., et al. 2012, MNRAS, 424, 1614
Omont, A., Cox, P., Bertoldi, F., et al. 2001, A&A, 374, 371
Pilbratt, G. L., Riedinger, J. R., Passvogel, T., et al. 2010, A&A, 518, L1
Poglitsch, A., Waelkens, C., Geis, N., et al. 2010, A&A, 518, L2
Ranalli, P., Comastri, A., & Setti, G. 2003, A&A, 399, 39
Reeves, J. N., O'Brien, P. T., Braito, V., et al. 2009, ApJ, 701, 493
Ricci, C., Trakhtenbrot, B., Koss, M. J., et al. 2017, Natur, 549, 488
Rieke, G. H., Young, E. T., Engelbracht, C. W., et al. 2004, ApJS, 154, 25
Rosario, D. J., McIntosh, D. H., van der Wel, A., et al. 2015, A&A, 573, A85
Rosario, D. J., Santini, P., Lutz, D., et al. 2012, A&A, 545, A45
Roseboom, I. G., Oliver, S. J., Kunz, M., et al. 2010, MNRAS, 409, 48
Rowan-Robinson, M., Valtchanov, I., & Nandra, K. 2009, MNRAS, 397, 1326
Rupke, D. S. N., & Veilleux, S. 2011, ApJL, 729, L27
Scoville, N., Aussel, H., Brusa, M., et al. 2007, ApJS, 172, 1
Shankar, F. 2009, NewAR, 53, 57
Shields, G. A., & Salviander, S. 2009, in ASP Conf. Ser. 419, Galaxy Evolution: Emerging Insights and Future Challenges, ed. S. Jogee et al. (San Francisco, CA: ASP), 392
Shimizu, T. T., Mushotzky, R. F., Meléndez, M., et al. 2017, MNRAS, 466, 3161

Siebenmorgen, R., Heymann, F., & Efstathiou, A. 2015, A&A, 583, A120
Silk, J., & Nusser, A. 2010, ApJ, 725, 556
Smith, D. J. B., Jarvis, M. J., Lacy, M., & Martínez-Sansigre, A. 2008, MNRAS, 389, 799
Somerville, R. S., Hopkins, P. F., Cox, T. J., Robertson, B. E., & Hernquist, L. 2008, MNRAS, 391, 481
Stalevski, M., Ricci, C., Ueda, Y., et al. 2016, MNRAS, 458, 2288
Stanley, F., Harrison, C. M., Alexander, D. M., et al. 2015, MNRAS, 453, 591
Stern, D. 2015, ApJ, 807, 129
Stern, D., Eisenhardt, P., Gorjian, V., et al. 2005, ApJ, 631, 163
Stevens, J. A., Jarvis, M. J., Coppin, K. E. K., et al. 2010, MNRAS, 405, 2623
Sturm, E., González-Alfonso, E., Veilleux, S., et al. 2011, ApJL, 733, L16
Symeonidis, M., Giblin, B. M., Page, M. J., et al. 2016, MNRAS, 459, 257
Treister, E., Cardamone, C. N., Schawinski, K., et al. 2009, ApJ, 706, 535
Treister, E., Krolik, J. H., & Dullemond, C. 2008, ApJ, 679, 140

Treister, E., Schawinski, K., Urry, C. M., & Simmons, B. D. 2012, ApJL, 758, L39
Treister, E., Urry, C. M., Chatzichristou, E., et al. 2004, ApJ, 616, 123
Tristram, K. R. W., Meisenheimer, K., Jaffe, W., et al. 2007, A&A, 474, 837
Tristram, K. R. W., Raban, D., Meisenheimer, K., et al. 2009, A&A, 502, 67
Urry, C. M., & Padovani, P. 1995, PASP, 107, 803
Vignali, C., Brandt, W. N., Schneider, D. P., & Kaspi, S. 2005, AJ, 129, 2519
Volonteri, M. 2010, A&ARv, 18, 279
Volonteri, M., Capelo, P. R., Netzer, H., et al. 2015, MNRAS, 452, L6
Volonteri, M., Haardt, F., & Madau, P. 2003, ApJ, 582, 559
Weisskopf, M. C., Brinkman, B., Canizares, C., et al. 2002, PASP, 114, 1
Werner, M. W., Roellig, T. L., Low, F. J., et al. 2004, ApJS, 154, 1
Winter, L. M., Mushotzky, R. F., Reynolds, C. S., & Tueller, J. 2009, ApJ, 690, 1322
Xue, Y. Q., Brandt, W. N., Luo, B., et al. 2010, ApJ, 720, 368